Controlled Individual Skyrmion Nucleation at Artificial Defects Formed by Ion Irradiation

Kayla Fallon, Sean Hughes, Katharina Zeissler, William Legrand, Fernando R Ajejas, Davide Maccariello, Samuel Mcfadzean, William A. P. Smith, Damien Stephen Mcgrouther, Sophie Collin, et al.

▶ To cite this version:

Kayla Fallon, Sean Hughes, Katharina Zeissler, William Legrand, Fernando R Ajejas, et al.. Controlled Individual Skyrmion Nucleation at Artificial Defects Formed by Ion Irradiation. Small, 2020, pp.1907450. 10.1002/smll.201907450 . hal-02500770

HAL Id: hal-02500770
https://hal.science/hal-02500770v1

Submitted on 6 Mar 2020

Controlled Individual Skyrmion Nucleation at Artificial Defects Formed by Ion Irradiation

*Kayla Fallon, Sean Hughes, Katharina Zeissler, William Legrand, Fernando Ajejas, Davide Maccariello, Samuel McFadzean, William Smith, Damien McGrouther, Sophie Collin, Nicolas Reyren, Vincent Cros, Christopher H. Marrows, and Stephen McVitie**

Kayla Fallon, Sean Hughes, Dr. Samuel McFadzean, William Smith, Dr. Damien McGrouther, Prof. Stephen McVitie
SUPA School of Physics and Astronomy, University of Glasgow, Glasgow, G12 8QQ, United Kingdom
E-mail: Stephen.McVitie@glasgow.ac.uk

Dr. Katharina Zeissler,[+] Prof. Christopher H. Marrows
School of Physics and Astronomy, University of Leeds, Leeds, LS2 9JT, United Kingdom

Dr. William Legrand, Dr. Fernando Ajejas, Dr. Davide Maccariello, Dr. Nicolas Reyren, Dr. Vincent Cros
Unité Mixte de Physique, CNRS, Thales, Univ. Paris-Sud, Université Paris-Saclay, 91767, Palaiseau, France

[+] Present address: Current address: National Physical Laboratory, Hampton Road, Teddington, TW110LW, United Kingdom

Keywords: Magnetic multilayers, magnetic skyrmions, skyrmion nucleation, ion irradiation, Lorentz microscopy

Magnetic skyrmions are particle-like deformations in the magnetic texture. They have great potential as information carriers in spintronic devices because of their interesting topological properties and favourable motion under spin currents. This paper reports a new method of nucleating skyrmions at nanoscale defect sites, created in a controlled manner with focused ion beam irradiation, in polycrystalline magnetic multilayer samples with an interfacial Dzyaloshinskii-Moriya interaction. This new method has three notable advantages: 1) localisation of nucleation; 2) stability over a larger range of external field strengths, including stability at zero field; and 3) existence of skyrmions in material systems where, prior to defect fabrication, skyrmions were not previously obtained by field-cycling. Additionally, it is observed that the size of defect nucleated skyrmions is uninfluenced by the defect itself - provided that the artificial defects are controlled to be smaller than the inherent skyrmion size. All of these characteristics are expected to be useful towards the goal of realising a skyrmion-

based spintronic device. This phenomenon is studied with a range of transmission electron microscopy techniques to probe quantitatively the magnetic behaviour at the defects with applied field and correlate this with the structural impact of the defects.

1. Introduction

A magnetic skyrmion is a quasiparticle of magnetisation characterised by its non-trivial topology. They appear in systems with a Dzyaloshinski-Moriya interaction (DMI) - which occurs when there is both a lack of inversion symmetry and strong spin-orbit coupling.[1, 2] Skyrmions were first observed in bulk B20 materials (such as MnSi and FeGe[3, 4]) and were found to be great candidates for low energy spintronic devices owing to their small size, stability and high mobility under spin-polarised currents.[5, 6] Recent research efforts have centred on finding a material system capable of nucleating individual skyrmions at room temperature and low magnetic fields with the aim of realising a skyrmion-based spintronic device.

DMI is also present at the interface between a ferromagnet and a heavy metal - where the interface itself breaks the inversion symmetry and the heavy metal provides a large spin-orbit interaction.[7–9] Pt/Co/Ir is a good example of an interface system where the DMI can reach the high value of 2 $\mathrm{mJm^{-2}}$, here the asymmetric heavy metal interfaces either side of the magnetic material serve to effectively boost the DMI.[11–13] This type of interfacial DMI - which enables the use of polycrystalline materials - allows for easily-deposited, tunable DMI systems in which skyrmions have been observed at room temperature.[12, 14–18]

One crucial step necessary for realising a skyrmion-based device lies in finding a reliable and controllable method of nucleating individual skyrmions. A multitude of nucleation methods have been proposed in recent years and these can be put into three categories based on: electrical currents,[10,19–24] laser pulses,[25–27] and locally applied electric fields.[28, 29] Skyrmions can also nucleate at naturally occurring defects in the material;[30, 31] however in this case there is little control over the formation of skyrmions due the random location and variable character of natural defects.

In this paper, we propose an original method of nucleating skyrmions using a focused ion beam (FIB) microscope to create nanoscale artificial defects. In Pt/Co based multilayers, ion irradiation is well-documented to both reduce the perpendicular anisotropy and increase the coercivity in a dose-dependent manner.[34–38] These effects have been exploited to engineer or tailor the local behaviour of magnetic systems.[39–41] For example a study found that extended circular areas of FIB irradiation (diameter 300 nm to 1 μm) in multilayers of Pt/Co can stabilise anti-skyrmions and Bloch skyrmions.[41] In contrast to the aforementioned study, here we propose point-like FIB-induced defects to nucleate Néel-type skyrmions.

2. Results

To explore artificial defects as a mechanism for skyrmion nucleation, point-like defects were created on two distinct multilayered Pt/Co based systems. As will be demonstrated shortly, in their 'as-deposited' state, one of these samples has a high magnetic remanence (close to M_s) and supports both skyrmions and Néel-type walls where the other has a low magnetic remanence (close to zero) and supports only Néel walls (in the field-driven regime). Both samples were prepared by dc magnetron sputtering and the layer structure is outlined in the following list, where the bracketed numbers are the layer thicknesses in nm and the subscript number is the number of repeat layers:

1. $\mathrm{Pt(10)/[Ir(1)/Co(0.6)/Pt(1)]_{\times10}/Pt(3)}$;
2. $\mathrm{Ta(10)/Pt(7.4)[Pt(0.6)/Co(1.2)/Ru(1.4)]_{\times5}/Pt(3)}$.

Studying two samples with slightly different layer composition and magnetic behaviour provides a useful test of the reproducibility of this nucleation method while also demonstrating the sensitivity of the method to the multilayer structure.

For transmission electron microscopy (TEM) studies the samples were deposited on substrates with an electron transparent Si_3N_4 window suspended from a thicker Si frame. Alternating gradient field magnetometry confirms all samples to support magnetisation out of the sample plane, as is promoted by the interface-induced perpendicular magnetic anisotropy (PMA).[42]. Artificial defects were made with a FEI Nova NanoLab 200 scanning electron microscope (SEM) and FIB. The samples were studied using a JEOL ARM200cF TEM, optimised for magnetic imaging, operated at 200kV.[43] *In situ* magnetising experiments were performed (at room temperature) on samples 1 and 2 using the Fresnel mode of Lorentz TEM to explore the behaviour of the samples with applied field before and after defect creation. Details of the magnetic textures at the defects in sample 1 were studied with quantitative, high resolution differential phase contrast (DPC) images. For multilayer materials with PMA, DPC imaging is enabled through advanced processing allowed by pixelated detectors[44–46] - this work uses the Medipix3 hybrid pixelated detector, with a Merlin readout system, from Quantum Detectors Ltd. We also explore the structural impact of the defects both in plan-view with bright field (BF) images and in cross-section with high angle annular dark field (HAADF) images taken from sample 1. The different TEM imaging modes will be discussed later in the paper.

In **Figure 1**, we show snapshots of the behaviour representative of samples 1 and 2 (unmodified by FIB) in an out-of-plane applied magnetic field in a series of Fresnel images. In the Fresnel mode of Lorentz TEM, magnetic contrast is visible as either bright or dark lines at the position of domain walls. For these samples with PMA and Néel-type walls the sample must be tilted to get contrast from the out of plane domains.[45–47] The electron transparent window on sample 2 is significantly buckled, this surface contortion provides local tilt when the sample is notionally ‘untilted’ with respect to the thicker flat Si frame as detailed previously.[46] For example in Figure 1(a) and (b) from sample 1 (flat surface), contrast is provided by tilting the sample 20° with respect to the sample plane. Conversely Figure 1(c) and (d) from sample 2 (buckled surface), were acquired with no explicit sample tilt but the images show clear magnetic contrast indicative of local film tilting. In the TEM we perform in situ magnetising experiments using the objective lens of the microscope, which allows application of an out of plane field variable between 10 mT (the remanent field of the lens) and 2 T. Fields below the remanent value must be set individually using specialised hardware external to the TEM.The Fresnel images in Figure 1 show discrete points in the reversal of the magnetisation from saturation in an out of plane positive field to saturation in a negative field. Without defects, sample 1 supports skyrmions just before saturation, Figure 1(b), after passing through the labyrinth-like coercive state, Figure 1(a). Néel type skyrmions are visible in Fresnel images as dot-like objects with contrast which is dark on one side and bright on the other; a red arrow above the skyrmions highlights their presence in Figure 1(b). The skyrmions 'naturally' supported by sample 1 are first stabilised in an applied field of -50 mT with a mean diameter of 170±20 nm, decreasing to 150±20 nm in a -80 mT field. The skyrmion diameter can be quantitatively measured from Fresnel images as the difference in the position of the extremas of bright and dark contrast - this property is unaffected by the image defocus, here ≈10 mm. By -90 mT the skyrmions are annihilated and the sample saturated. Sample 1 has a high magnetic remanence - upon increasing the applied field from negative saturation towards positive saturation, no domains form until the sample is in a field of +20 mT. Without defects, skyrmions are not observed in sample 2. It also has a dense labyrinth-like coercive state, Figure 1(c), but as the field strength is increased the domains shrink to sparse thread-like objects with long domain walls pairs separated by ≈150 nm, Figure 1(d). By -100 mT the sample has saturated with no intermediate skyrmion state observed. Sample 2 has a magnetic remanence of almost zero and when the field is increased again towards positive saturation, domains begin to form just before -10 mT.

As discussed earlier, FIB irradiation can alter the magnetic and structural properties of magnetic multilayer films. To explore this effect for skyrmion nucleation, FIB defects were made using a FEI Nova NanoLab 200 scanning electron microscope (SEM) and FIB with a 30 keV Ga^+ beam energy and beam current of 10 pA - giving an ion beam diameter of 10 nm. This diameter is defined as the probe full width half maximum (FWHM), but the probe has extensive tails over a larger distance leading to FIB defined features larger than the quoted beam diameter.[40] A wide range of defects were made on sample 1 with the geometry shown in **Figure 2**(a) with the beam normal to the sample surface. The irradiation was controlled to deliver a dose between 10^{14} and 10^{18} ions/cm^2. To precisely control the ion dose (and to fabricate the smallest possible defects) direct machine commands were used to irradiate precisely one spot of the sample with the ion beam. More technical details related to the creation of point-like FIB defects are provided in the supporting information.

The structural impact of the defects on sample 1 has been studied in both plan view, with BF images, and in cross-section, with HAADF images. For the plan view study, spot defects were made on sample 1. Conversely, for the cross-sectional study, line defects (of equivalent dose to the spot defects) were made on the thicker Si frame of sample 1. A cross-sectional electron transparent lamella was prepared from this region using a Xe^+ plasma FIB. To protect the sample from damage during the fabrication process, the region was first coated with carbonaceous platinum.

A selection of BF and HAADF images from defect sites created with different ion dose are shown in Figure 2. The top row of Figure 2 shows the BF images in which the granular structure of the polycrystalline sample is visible. The bottom row shows the HAADF images in which the discrete layer structure of the sample is visible. HAADF imaging is essentially atomic number Z imaging, where brighter image contrast corresponds to a higher Z material, hence in these images, in the area corresponding to the multilayer, Ir and Pt are bright (Z = 77, 78 respectively) and Co is dark (Z = 27). A defect of dose 1×10^{16} ions/cm^2 is shown in the first column of images, Figure 2(b,e). There is little evidence of damage from this defect in the HAADF image, with each layer of the structure resolvable, similarly the centre of the BF image shows some slight grain enlargement - a known effect of ion irradiation on polycrystalline films[51] - but no grain growth out with the normal distribution of sizes. The 5×10^{16} ions/cm^2 defect causes visible damage to the layer structure, Figure 2(f): there is intermixing of the layers in a 'u'-shape extending across a distance of 70 nm in the top layers and to a depth of up to ≈ 7 layers at the centre of the defect. Intermixing is identified by loss of the black/white alternating layer contrast. The corresponding BF image shows similar grain growth to the 1×10^{16} ions/cm^2 defect. There is a considerable area of grain enlargement associated with the 1×10^{17} ions/cm^2 defect, Figure 2(g), and the layer structure has been erased over a distance of 80 nm - additionally this defect causes milling of 6-7 nm into the sample, judging by the infill of the protective layers as marked by the white dashed line overlaid on Figure 2(g). It is noted that defects smaller than 10^{16} ions/cm^2 show no visible signs of damage when judged by the grain size and the uniformity of the layer structure. Defects created with doses larger than 10^{18} ions/cm^2 resulted in clearly defined holes through the multilayer stack due to milling.

Figure 3(a) shows a Fresnel image of sample 1, patterned with an array of ≈ 250 nm diameter defects (ion dose 10^{17} ions/cm^2). The image was acquired in a zero-field environment at room temperature after application of a saturating field. Strikingly, single skyrmions can be observed at many of the defect sites. Compared to the spot defects in Figure 3 these are extended defects (created with a different method as explained in the FIB patterning section of the Supporting Information), purposed in this section for two reasons: to demonstrate the separation of nonmagnetic defect contrast and magnetic skyrmion contrast; and to evaluate the relationship between defect size and skyrmion size.

Figures 3(b) and (c) illustrate the contrast from the top left defect site in (a) with and without a skyrmion respectively. The changed physical structure of the defect results in non-magnetic image contrast even after the skyrmion has been removed (by saturating the defect site) as shown in Figure 3(c). The line traces taken from the defects are shown in Figure 3(d).

These indicate that the contrast from a saturated defect site is symmetric compared to a defect site with a skyrmion. Moreover, the magnetic contrast in these images is generated by the sample tilt (here +20°), hence any magnetic contrast will reverse with tilt, i.e. at -20° black becomes white and vice versa. Hence, these differences in contrast allow defects and skyrmions to be easily distinguished from one another. Also indicated on Figure 3(d) is the defect diameter and the skyrmion diameter. As mentioned above, the mean defect diameter (averaged over multiple defect sites) is 250±30 nm while the mean skyrmion diameter (in zero field) is 300±10 nm. The similarity between the defect size and skyrmion size suggests that the skyrmion size could be linked to the defect size. For defects smaller than the 'natural' skyrmion size we observe a different relationship, but we discuss this in detail later.

To be technologically advantageous the defects should cause a minimal increase to the depinning current required to move a skyrmion from the defect site. Whilst this is not studied here directly, it is known that local changes in anisotropy increase the pinning field,[23] and that higher ion doses cause a larger modification of the anisotropy.[34–38] Hence, we determine the lowest dose required to cause low-field, room-temperature nucleation for samples 1 and 2. The enlargement of the grains is thought less likely to be problematic as a previous study identifies the most severe pinning for grain sizes which are the same size as the skyrmions[23] and the FIB enlarged grains are still an order of magnitude smaller than the skyrmions.

Sample 1 was irradiated with ten different doses between 10^{14} and 10^{18} ions/cm^2, with five repetitions of each. Similarly, sample 2 was irradiated with doses between 10^{12} and 10^{16} ions/cm^2. These were spot defects created by irradiating precisely one position on the sample with the FIB probe. The charts in **Figure 4** summarise the field behaviour of the magnetisation at each type of defect site on (a) sample 1 and (b) sample 2. Note that on Figure 4(a) the field scale is not linear between ±10.8 mT as the objective lens field cannot be varied smoothly between these values. Doses below 5×10^{16} ions/cm^2 on sample 1 and below 5×10^{15} ions/cm^2 on sample 2 showed no nucleation activity and are not included in the charts. The lightest colour indicates that all defect sites of a given dose are are unchanged from a magnetically saturated state, while the darkest colour indicates that all defect sites of a given dose have a magnetic object local to the defect. The icon inset on each square indicates the nature of the magnetic object local to the defect: a circle indicates all occupied sites have skyrmions; a bean shape indicates all occupied sites have expanded domains; both a circle and bean indicate a mixture of the above; and the maze icon indicates the sample is in a state close to remanence with labyrinth domains (as in Figure. 1(a) and (c)) where it is meaningless to evaluate the behaviour local to the defect sites. The description ‘expanded domain’ refers to a bubble that has an extended size, only compact magnetic objects have been identified as skyrmions - examples of both are marked in the Fresnel image in Figure 4. Expanded domains are also present, together with skyrmions, in the Fresnel image in Figure 1(b) which shows sample 1, unmodified, in a field of -80 mT. To be clear, objects are classified as skyrmions if they are circular with simple bright-dark contrast, where, alternatively, structures are classified as expanded domains if they are associated with either a more complex contrast distribution or are elongated. Hence the areas of most interest (outlined in red) are those with a circle on a dark background, indicating all defect sites with that dose have stabilised skyrmions, i.e. 100% success rate of skyrmion nucleation.

The behaviour of the samples was again monitored as the applied field was lowered from saturation in a positive out of plane field to saturation in a negative field. Non-local to defect sites the magnetic reversal is the same as in the unmodified samples as discussed in relation to Figure 1. However, as highlighted in red, both samples have specific combinations of applied field and defect dose that cause local nucleation and retention of compact individual skyrmions at 100% of defect sites. **Table 1** provides details of the ‘ideal’ artificial defects found to cause 100% skyrmion nucleation in samples 1 and 2.

Critically, for sample 1 the field range of skyrmion stability includes zero applied field. Sample 2 exhibited very similar behaviour with dose and field to sample 1 although, as expected from a low magnetic remanence system, to retain compact skyrmions a bias field was required. This is a particularly interesting result as skyrmions were not observed at room temperature in sample 2 prior to defect creation. Furthermore, the dose required to nucleate skyrmions is an order of magnitude smaller for sample 2 compared to sample 1 - demonstrating the extreme sensitivity of this nucleation method to the sample structure. As seen in the cross-sectional images presented in Figure 2(f,g), the energy imparted in the sample by the ions causes damage and intermixing of the multilayer structure: alloying the multilayer. Given the different elemental composition of the two multilayer stacks studied, the magnetic properties of the resulting alloy are certainly different. For example, an older study[52] characterises the magnetisation of binary alloys of Co and various transition metals. It shows that the magnetisation of Co is more sensitive to alloying with Ru than either Ir or Pt - giving a possible explanation for the greater sensitivity of sample 2 to ion dose than sample 1.

From the spot defects on sample 1, the mean skyrmion size in zero field is 170 ± 30 nm at 5×10^{16} ions/cm^2 defects and 180 ± 30 nm at 1×10^{17} ions/cm^2 defects (details of these measurements are in the supporting information). From the structural imaging in Figure 2, on sample 1 these defects are associated with an area of damage around 100 nm in diameter. This is in stark contrast to the extended 250 nm diameter defects that nucleate 300 nm diameter skyrmions presented in Figure 3.

The defect nucleated skyrmions in sample 2 are around 300 nm in diameter. As no skyrmions were observed in sample 2 without defects there can be no direct comparison - however it is useful to consider the large difference in diameter of skyrmions measured from sample 2 compared to sample 1. The images of defects made on sample 2 show no visible non-magnetic phase contrast, like presented in the Fresnel image in Figure 3(c), or obvious grain growth, like shown in the BF images in Figure 2(b-d). Consequently, although not measured, the lateral size of the defects is almost certainly smaller than measured for sample 1 but the skyrmions are larger.

This information leads us to the conclusion that, for defects smaller than the ‘natural’ skyrmion size, the size of the defect nucleated skyrmions is determined by the sample properties and not the defect itself. The skyrmion size data relating to sample 1 (both unmodified and with artificial defects) and sample 2 is provided in full in the Supporting Information.

Differential phase contrast (DPC) images were taken of sample 1, and allow quantitative measurement of the saturation induction Bs of the film near a defect, where $B_s = \mu_0 M_s$. DPC is a scanning TEM technique where the Lorentz deflections of the electron beam are measured directly by measuring shifts in the unscattered central diffraction disk. For skyrmionic multilayer materials, DPC datasets must be acquired using a pixelated detector. The combination of perpendicular magnetisation (the samples must be tilted in order to cause any beam deflection) and large sample thickness compared to the active magnetic thickness mean these materials cause only a small beam deflection but generate considerable, undesirable diffraction contrast associated with the crystallites. This diffraction contrast completely masks the magnetic contrast in standard DPC, however, the more advanced processing enabled by pixelated detectors can reduce this contrast and allow for successful quantitative imaging with DPC.[44–46]

As outlined in existing studies,[45, 46] the beam Lorentz deflection angle β from perpendicularly magnetised materials depends on the sample tilt and is proportional to B_s. **Figure 5**(a) shows a DPC image from a 5×10^{16} ions/cm^2 defect site on sample 1 in a field of 10 mT. The contrast is from the magnetic induction associated with a circular skyrmion which is tilted with respect to the electron beam. The skyrmion is then imaged as an extended dipolar field. The light central area of Figure 5(a) shows where this dipolar field is strongest, and the width of this bright area (taken parallel to the tilt axis) corresponds to the diameter of the skyrmion, measured to be 150 nm. Diagrammatic descriptions are provided in the Supporting Information to aid interpretation of DPC images of Néel skyrmions. A white circle, diameter 70 nm, is overlaid at the position of the defect with size matching the area of physical damage associated with this dose, as identified from Figure 2(f). A line trace, averaged over 15 pixels, was taken from the area marked in Figure 5(a), near to the defect, and is shown next to the DPC image. By fitting a hyperbolic tangent function to this line trace, the deflection due to the domains was determined as 1.7±0.2 μrad (sample was tilted by 24.6°). From this B_s was calculated to be 1.2±0.1 T, assuming a total magnetic thickness of 6 nm resulting from ten 0.6 nm thick Co layers. This is compared to magnetometry measurements from this sample before irradiation which measured M_s as 1.0 ± 0.1 MAm^{-1} - equivalent to 1.2 ± 0.1 T. This quantitative analysis suggests that the defect has caused skyrmion nucleation in all layers, and not just in the surface layers most impacted by the irradiation.

3. Discussion and Conclusion

In this paper, we have demonstrated that nanoscale artificial defects (created with FIB irradiation) can be used to nucleate Néel-type, isolated, single skyrmions at precise locations in polycrystalline magnetic multilayer systems at room temperature in low, even zero, applied magnetic field. We have studied this effect in different multilayer systems and draw two interesting conclusions. Firstly, in samples that are known to support skyrmions, the defects create an additional pocket of skyrmion stability at a lower applied field strength than without artificial defects. In sample 1 as-grown, skyrmions are observed between -50 to -80 mT but with defects skyrmions are also stable between +15 to -5 mT. Secondly, as observed in sample 2, these artificial defects can even stabilise skyrmions in samples with lower DMI strength that naturally support homochiral Néel walls but never stabilise skyrmions on field-cycling alone.

The mobility of these FIB nucleated skyrmions remains to be studied. The structural imaging of the defects, Figure 2, indicates that nucleation is most successful at defects with partial layer intermixing - undoubtedly this intermixing is associated with local lowering of the perpendicular anisotropy and DMI strength as both originate from the layer interfaces. Both of these effects will likely increase the depinning field, as will the local reduction in M_s predicted by alloying.[23, 52]

We note that the size of the skyrmions nucleated appears uninfluenced by the defect itself so long as it is smaller than the inherent skyrmion size. The skyrmion size in a multilayer system is determined by the interplay of various magnetic energy terms controlled by: the strength of the DMI, the anisotropy, the exchange stiffness and the saturation magnetisation of the material.[17] Hence, even though the skyrmions observed in this study are on the order of 100 nm, we expect this nucleation method to successfully nucleate technologically relevant sub-100 nm skyrmions in an optimised material system. To this end we note that it is possible to create smaller FIB defect sites; for example, here we used a 30 keV, 10 pA focused Ga^+ beam which has a beam diameter of ≈10 nm but a 35 keV, 10 pA focused He^+ beam has a beam diameter an order of magnitude smaller and can mill sub-10 nm features.[53, 54]

It is expected that new device technologies are more likely to be utilised if they mould into current fabrication methods. A relevant example is that, to support skyrmions, polycrystalline systems are desirable over single crystal systems as they fit with current deposition technologies. Focused ion beam microscopes are widely used in device fabrication (for example in fabrication of semiconductor devices and disk read/write heads) hence controlled skyrmion nucleation at artificial FIB defects is certainly a promising mechanism for reproducible generation of room-temperature, zero-field skyrmions.

Experimental Section

Sample preparation: Sample 1 was prepared at the University of Leeds by dc magnetron sputtering using a base pressure of 2×10^{-8} mbar and an Ar pressure of 6.7 mbar during deposition. Sample 2 was prepared at CNRS/Thalés by dc magnetron sputtering using a base pressure of 8×10^{-8} mbar and an Ar pressure during deposition of 2.5×10^{-3} mbar. Both samples were deposited on top of Pt buffers to control the perpendicular magnetic anisotropy and are capped with Pt to prevent oxidation. Magnetic characterisation of the samples prior to defect formation was done using SQUID and AGFM. Artificial defects were created using a FEI Nova NanoLab 200 SEM and FIB using a 30 kV Ga^+ beam energy and 10 pA current. The patterning method used to fabricate the defects is discussed in detail in the supplementary information. The cross-sectional lamella was fabricated (from an area containing pre-made artificial defects) using a standard procedure on a FEI Helios SEM and FIB using a 30 kV Xe^+ beam energy before a final polish was performed with a 5 kV beam energy.

TEM imaging: All TEM imaging was performed on a JEOL ARM 200cF equipped with a cold field emission gun and CEOS probe aberration corrector. The HAADF images were collected in ‘objective on’ mode using spot size 5, a 40 µm condenser 1 aperture (convergence angle 36 mrad) and a 2 cm camera length. These conditions give a probe size of < 0.2 nm and the HAADF images presented in this paper have a sampling pixel size of 0.2 nm. For the Lorentz TEM images microscope was operated in ‘objective-off’ mode. The Fresnel images are taken with the instrument in TEM mode with a defocus between 5 and 10 mm. The DPC images are taken with the instrument in STEM mode. The DPC dataset was collected using the Medipix3 hybrid pixelated detector with a Merlin readout system. The DPC image shown in this paper was taken using spot size 1, a 20 µm condenser 1 aperture (convergence angle 1 mrad) and a 1500 cm camera length. This gives a probe size of 3 nm and, in the DPC image presented, the sampling pixel size is 3 nm.

Data availability: Data associated with this work is available from the University of Glasgow: Enlighten Data repository under a CC-BY license at [URL tbc].

Supporting Information

Supporting Information is available from the Wiley Online Library or from the author.

Acknowledgements

The authors acknowledge financial support from European Union grant MAGicSky No. FETOpen-665095; and from the EPSRC through grants EP/M024423/1 and EP/P001483/1; and from the Agence Nationale de la Recherche, France, under Grant Agreement No. ANR-17-CE24-0025 (TOPSKY).

Received: ((will be filled in by the editorial staff))
Revised: ((will be filled in by the editorial staff))
Published online: ((will be filled in by the editorial staff))

References

[1] I. Dzyaloshinsky, *J. Phys. Chem. Solids* **1958**, *4*, 241–255.

[2] T. Moriya, *Phys. Rev.* **1960**, *120*, 91–98.

[3] S. Mühlbauer, B. Binz, F. Jonietz, C. Pfleiderer, A. Rosch, A. Neubauer, R. Georgii, P. Böni, *Science* **2009**, *323*, 915–920.

[4] X. Z. Yu, Y. Onose, N. Kanazawa, J. H. Park, J. H. Han, Y. Matsui, N. Nagaosa, Y. Tokura, *Nature* **2010**, *465*, 901–904.

[5] X. Z. Yu, N. Kanazawa, W. Z. Zhang, T. Nagai, T. Hara, K. Kimoto, Y. Matsui, Y. Onose, Y. Tokura, *Nat. Commun.* **2012**, *3*.

[6] F. Jonietz, S. Mühlbauer, C. Pfleiderer, A. Neubauer, W. Münzer, A. Bauer, T. Adams, R. Georgii, P. Böni, R. A. Duine, K. Everschor, M. Garst, A. Rosch, *Science* **2011**, 1648–1652.

[7] M. Bode, M. Heide, K. Von Bergmann, P. Ferriani, S. Heinze, G. Bihlmayer, A. Kubetzka, O. Pietzsch, S. Blügel, R. Wiesendanger, *Nature* **2007**, *447*, 190–193.

[8] S. Heinze, K. Von Bergmann, M. Menzel, J. Brede, A. Kubetzka, R. Wiesendanger, G. Bihlmayer, S. Blügel, *Nat. Phys.* **2011**, *7*, 713–718.

[9] A. Fert, N. Reyren, V. Cros, *Nat. Rev. Mater.* **2017**, *2*, 17031.

[10] N. Romming, C. Hanneken, M. Menzel, J. E. Bickel, B. Wolter, K. Bergmann, A. Kubetzka, R. Wiesendanger, *Science* **2013**, *341*, 636–639.

[11] A. Hrabec, N. A. Porter, A. Wells, M. J. Benitez, G. Burnell, S. McVitie, D. McGrouther, T. A. Moore, C. H. Marrows, *Phys. Rev. B* **2014**, *90*, 020402.

[12] C. Moreau-Luchaire, S. C. Mouta, N. Reyren, J. Sampaio, C. A. Vaz, N. Van Horne, K. Bouzehouane, K. Garcia, C. Deranlot, P. Warnicke, P. Wohlhüter, J. M. George, M. Weigand, J. Raabe, V. Cros, A. Fert, *Nat. Nanotechnol.* **2016**, *11*, 444–448.

[13] K. Zeissler, M. Mruczkiewicz, S. Finizio, J. Raabe, P. M. Shepley, A. V. Sadovnikov, S. A. Nikitov, K. Fallon, S. McFadzean, S. McVitie, T. A. Moore, G. Burnell, C. H. Marrows, *Sci. Rep.* **2017**, *7*, 1–9.

[14] A. Soumyanarayanan, M. Raju, A. L. Oyarce, A. K. Tan, M. Y. Im, A. P. Petrovic, P. Ho, K. H. Khoo, M. Tran, C. K. Gan, F. Ernult, C. Panagopoulos, *Nat. Mater.* **2017**, *16*, 898–904.

[15] S. Woo, K. Litzius, B. Krüger, M. Y. Im, L. Caretta, K. Richter, M. Mann, A. Krone, R. M. Reeve, M. Weigand, P. Agrawal, *Nat. Mater.* **2016**, *15*, 501–506.

[16] G. Yu, P. Upadhyaya, X. Li, W. Li, S. K. Kim, Y. Fan, K. L. Wong, Y. Tserkovnyak, P. K. Amiri, K. L. Wang, *Nano Lett.* **2016**, *16*, 1981–1988.

[17] O. Boulle, J. Vogel, H. Yang, S. Pizzini, D. de Souza Chaves, A. Locatelli, T. O. Menteş, A. Sala, L. D. Buda-Prejbeanu, O. Klein, M. Belmeguenai, *Nat.Nanotechnol.* **2016**, *11*, 449–454.

[18] K. Zeissler, S. Finizio, K. Shahbazi, J. Massey, F. A. Ma'Mari, D. M. Bracher, A. Kleibert, M. C. Rosamond, E. H. Linfield, T. A. Moore, J. Raabe, G. Burnell, C. H. Marrows, *Nat. Nanotechnol.* **2018**, *13*, 1161–1166.

[19] J. Sampaio, V. Cros, S. Rohart, A. Thiaville, A. Fert, *Nat. Nanotechnol.* **2013**, *8*, 839–844.

[20] J. Iwasaki, M. Mochizuki, N. Nagaosa, *Nat. Nanotechnol.* **2013**, *8*, 742–747.

[21] W. Jiang, P. Upadhyaya, W. Zhang, G. Yu, M. B. Jungfleisch, S. G. E. Velthuis, A. Hoffmann, *Science* **2015**, *349*, 1–21.

[22] A. Hrabec, J. Sampaio, M. Belmeguenai, I. Gross, R. Weil, S. M. Cherif, A. Stashkevich, V. Jacques, A. Thiaville, S. Rohart, *Nat. Commun.* **2017**, *8*, 15765.

[23] W. Legrand, D. Maccariello, N. Reyren, K. Garcia, C. Moutafis, C. Moreau-Luchaire, S. Collin, K. Bouzehouane, V. Cros, A. Fert, *Nano Lett.* **2017**, *17*, 2703–2712.

[24] S. Finizio, K. Zeissler, S. Wintz, S. Mayr, T. Weßels, A. J. Huxtable, G. Burnell, C. H. Marrows, J. Raabe, *Nano. Lett.* **2019**, *19*, 7246–7255.

[25] T. Ogasawara, N. Iwata, Y. Murakami, H. Okamoto, Y. Tokura, *Appl. Phys. Lett.* **2009**, *94*, 1–4.

[26] M. Finazzi, M. Savoini, A. R. Khorsand, A. Tsukamoto, A. Itoh, L. Dùo, A. Kirilyuk, T. Rasing, M. Ezawa, *Phys. Rev. Lett.* **2013**, *110*, 1–5.

[27] S. G. Je, P. Vallobra, T. Srivastava, J. C. Rojas-Sánchez, T. H. Pham, M. Hehn, G. Malinowski, C. Baraduc, S. Auffret, G. Gaudin, S. Mangin, H. Béa, O. Boulle, *Nano Lett.* **2018**, *18*, 7362–7371.

[28] P. J. Hsu, A. Kubetzka, A. Finco, N. Romming, K. Von Bergmann, R. Wiesendanger, *Nat. Nanotechnol.* **2017**, *12*, 123–126.

[29] T. Srivastava, M. Schott, R. Juge, V. Křižáková, M. Belmeguenai, Y. Roussigné, A. Bernand-Mantel, L. Ranno, S. Pizzini, S. M. Chérif, A. Stashkevich, *Nano Lett.* **2018**, *18*, 4871–4877.

[30] F. Büttner, I. Lemesh, M. Schneider, B. Pfau, C. M. Günther, P. Hessing, J. Geilhufe, L. Caretta, D. Engel, B. Krüger, J. Viefhaus, S. Eisebitt, G. S. Beach, *Nat. Nanotechnol.* **2017**, *12*, 1040–1044.

[31] S. Woo, Y. Zhou, K. M. Song, B.-C. Min, J. Raabe, X. Zhang, K.-Y. Lee, J. Chang, X. Liu, M.-C. Park, M. Weigand, M. Ezawa, J. W. Choi, S. Finizio, H. C. Koo, *Nat. Electron.* **2018**, *1*, 288–296.

[32] V. M. Uzdin, M. N. Potkina, I. S. Lobanov, P. F. Bessarab, H. Jónsson, *Physica B: Condens. Matter* **201**8, *549*, 6-9.

[33] L. Desplat, D. Suess, J.-V. Kim, R. L Stamps, *Phys. Rev. B* **2018**, *9*8, 134407.

[34] C. Chappert, H. Bernas, J. Ferré, V. Kottler, J.-P. Jamet, Y. Chen, E. Cambril, T. Devolder, F. Rousseaux, V. Mathet, H. Launois, *Science* **1998**, *280*, 1919–1922.

[35] C. T. Rettner, S. Anders, J. E. Baglin, T. Thomson, B. D. Terris, *Appl. Phys. Lett.* **2002**, *80*, 279–281.

[36] C. Vieu, J. Gierak, H. Launois, T. Aign, P. Meyer, J. P. Jamet, J. Ferré, C. Chappert, T. Devolder, V. Mathet, H. Bernas, *J. Appl. Phys.* **2002**, *91*, 3103–3110.

[37] G. Kusinski, G. Thomas, *Microsc. Microanal.* **2002**, *8*, 319–332.

[38] J. Fassbender, D. Ravelosona, Y. Samson, *J. Phys. D* **2004**, *37*, R179–R196.

[39] A. Aziz, S. J. Bending, H. G. Roberts, S. Crampin, P. J. Heard, C. H. Marrows, *Phys. Rev. Lett.* **2006**, *97*, 206602.

[40] M. J. Benitez, M. A. Basith, R. J. Lamb, D. McGrouther, S. McFadzean, D. A. MacLaren, A. Hrabec, C. H. Marrows, S. McVitie, *Phys. Rev. Appl.* **2015**, *3*, 1–10.

[41] S. Zhang, A. K. Petford-Long, C. Phatak, *Sci. Rep.* **2016**, *6*, 1–10.

[42] G. H. O. Daalderop, P. J. Kelly, M. F. H. Schuurmans, *Phys. Rev. B* **1994**, *50*, 9989.

[43] S. McVitie, D. McGrouther, S. McFadzean, D. A. MacLaren, K. J. O. Shea, M. J. Benitez, *Ultramicroscopy* **2015**, *152*, 57–62.

[44] M. Krajnak, D. McGrouther, D. Maneuski, V. O. Shea, S. McVitie, *Ultramicroscopy* **2016**, *165*, 42–50.

[45] S. McVitie, S. Hughes, K. Fallon, S. McFadzean, D. McGrouther, M. Krajnak, W. Legrand, D. Maccariello, S. Collin, K. Garcia, N. Reyren, V. Cros, A. Fert, K. Zeissler, C. H. Marrows, *Sci. Rep.* **2018**, *8*, 5703.

[46] K. Fallon, S. McVitie, W. Legrand, F. Ajejas, D. Maccariello, S. Collin, V. Cros, N. Reyren, *Phys. Rev. B* **2019**, 100, 214431.

[47] M. J. Benitez, A. Hrabec, A. P. Mihai, T. A. Moore, G. Burnell, D. McGrouther, C. H. Marrows, S. McVitie, *Nat. Commun.* **2015**, *6*, 8957.

[48] A. Bogdanov, A. Hubert, *phys. stat. sol. (b)* **1994**, 186, 527

[49] A. O. Leonov, T. L. Monchesky, N. Romming, A. Kubetzka, A. N. Bogdanov, R. Wiesendanger, *New J. Phys.* **2016**, 18, 065003.

[50] N. Romming, A. Kubetzka, C. Hanneken, K. von Bergmann, R. Wiesendanger, *Phys. Rev. Lett.* **2015**, 114, 177203

[51] C. M. Park, J. A. Bain, *J. Appl. Phys.* **2002**, *91*, 6830–6832.

[52] J. Crangle, D. Parsons, *Proceedings of the Royal Society of London. Series A, Mathematical and Physical Sciences* **1960**, *255*, 509–19.

[53] N. Bassim, K. Scott, L. A. Giannuzzi, *MRS Bull.* **2014**, *39*, 317–325.

[54] G. Hlawacek, V. Veligura, R. van Gastel, B. Poelsema, *J. Vac. Sci. Technol. B* **2014**, *32(2).*

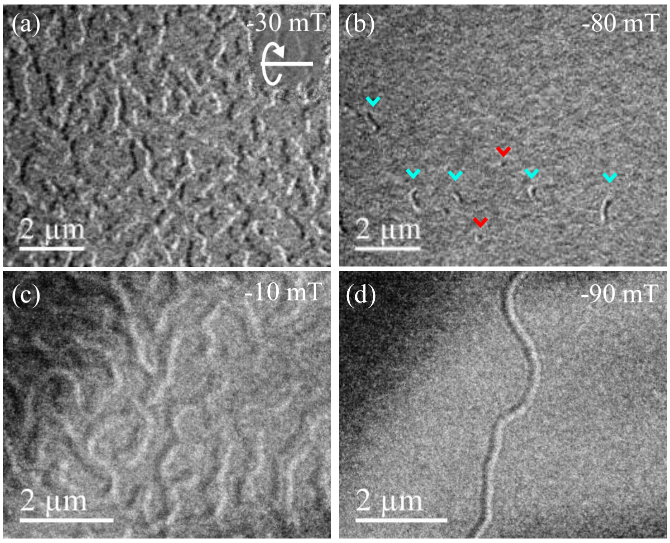

Figure 1. Fresnel images of sample 1 (tilted 20° about axis labelled) and 2 (tilt provided by surface contortion) in the as-grown state. For sample 1 the labyrinth-like state (a) must be passed to obtain skyrmions (mean diameter ≈ 150 nm) at a higher field (b) before saturation. The skyrmions are sparse and where present are highlighted by a red arrow above the skyrmion. Sample 2 also has a labyrinth-like coercive state (c), upon increasing the field strength towards saturation the domains become sparse and thread-like, with pairs of domain walls separated by ≈150 nm (d). No skyrmions are observed as the external field strength is increased and the sample saturates.

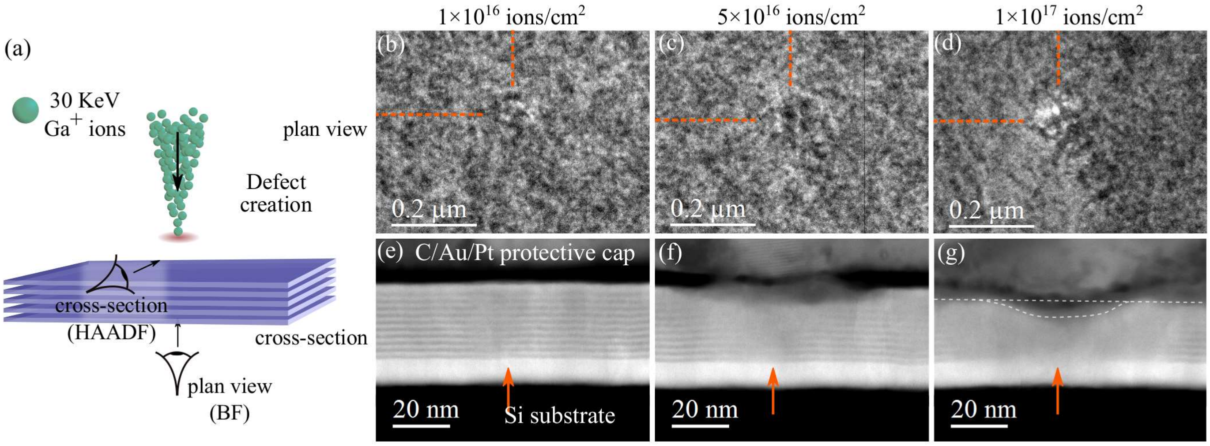

Figure 2. (a) schematic of FIB defect creation. Bright field (BF) images of the defects in plan view - looking straight down on the sample - in (b-d), and high angle annular dark field (HAADF) images of the defects in cross-section (e-g). The gradual erasing of the layer structure with increasing ion dose can be seen in HAADF images (e-g) - at 10^{16} ions/cm^2 the layer structure is mostly undisturbed, at 5×10^{16} ions/cm^2 there is a shallow ‘u’ shape with clear intermixing and at 10^{17} ions/cm^2 there is slight milling (highlighted by the white dashed lines) and no layer details remaining. The corresponding changes to the grain structure are seen in BF images (b-d). All images taken on sample 1 and the arrows on HAADF images and lines on BF images are to guide the eye to the centre of the defect.

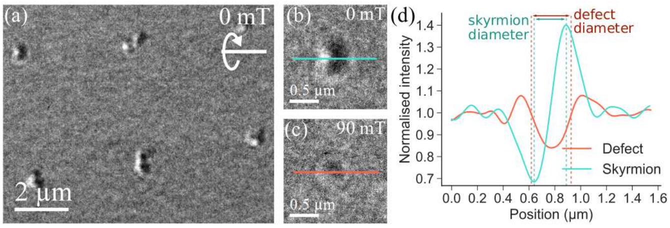

Figure 3. Fresnel image of sample 1 after creation of extended defects with ion dose 10^{17} ions/cm^2 in a field free environment - skyrmions are clearly visible at most defect sites. (b) enlarged image of a defect with skyrmion for comparison with (c) enlarged image of a saturated defect. Line trace in (d) indicates the distinction between a skyrmion and defect is easily made. All Fresnel images taken with sample tilt of 20° about the axis indicated.

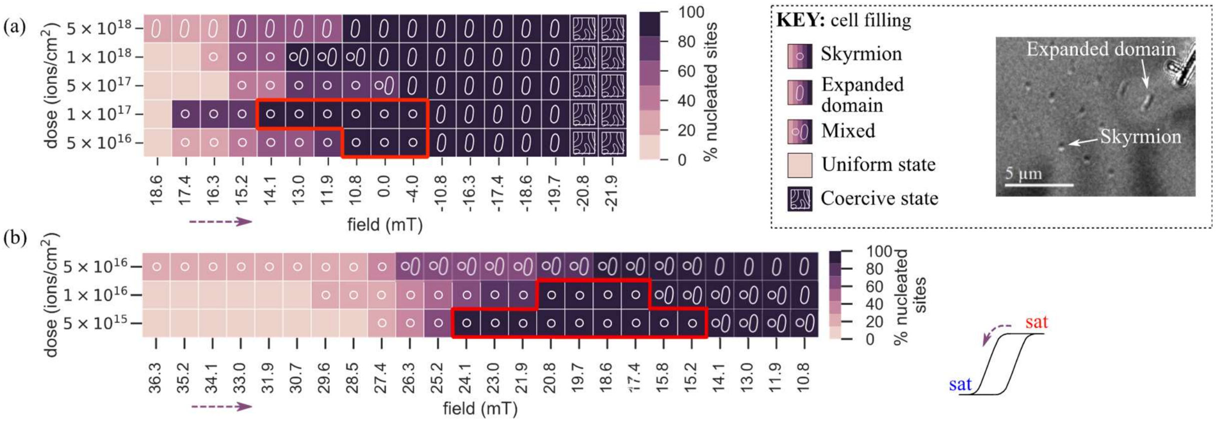

Figure 4. Charts presenting the detailed behaviour of defect sites as a function of ion dose and applied out of plane field on sample 1 in (a) and sample 2 in (b). These charts are explained by the colourbar and key. The Fresnel image, from sample 2, provides examples of the different magnetic states in the key. Squares outlined in red highlight the most interesting parts of the chart that have 100% skyrmion nucleation.

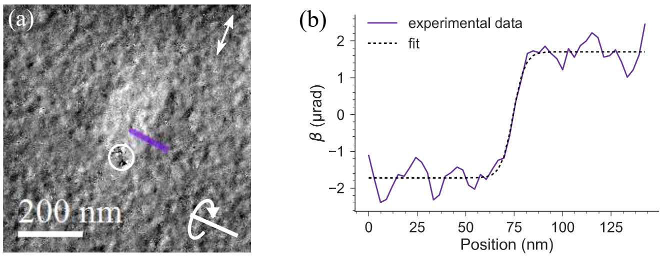

Figure 5. (a) DPC image of sample 1, tilted by ≈ 25° about the axis indicated, with a 150 nm skyrmion nucleated at a 5×10^{16} ions/cm^2 defect site. The component of magnetic induction mapped is indicated by the double-headed arrow inset top left. The circle gives the size and position of the defect and the line shows where the line trace (b) - averaged over 15 lines - was taken.

Table 1. Summary of artificial defect types that cause 100% skyrmion nucleation at room temperature - detailed is the dose associated with each successful defect and field range over which the nucleated skyrmions remain stable.

Sample	Defect dose (ions/cm^2)	Range of stability (mT)

1	5×10^{16}	+10.8 to -4.0
1	1×10^{17}	+14.1 to -4.0
2	5×10^{15}	+24.1 to +15.8
2	1×10^{16}	+20.8 to +17.4

The table of contents entry should be 50−60 words long and should be written in the present tense and impersonal style (i.e., avoid we). The text should be different from the abstract text.

Nanoscale artificial defects in magnetic multilayer films with PMA and DMI, made in a controllable manner using a FIB, offer deterministic skyrmion nucleation. The nucleated skyrmions are stable over a wider (and lower) range of external field values and the nucleation field is tunable with the type of defect fabricated.

Keyword skyrmions

Kayla Fallon, Sean Hughes, Katharina Zeissler, William Legrand, Fernando Ajejas, Davide Maccariello, Samuel McFadzean, William Smith, Damien McGrouther, Sophie Collin, Nicolas Reyren, Vincent Cros, Christopher H. Marrows, and Stephen McVitie*

Controlled Individual Skyrmion Nucleation at Artificial Defects Formed by Ion Irradiation

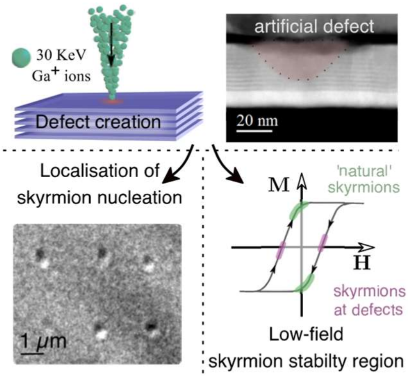

ToC figure

Supporting Information

Controlled Individual Skyrmion Nucleation at Artificial Defects Formed by Ion Irradiation

*Kayla Fallon, Sean Hughes, Katharina Zeissler, William Legrand, Fernando Ajejas, Davide Maccariello, Samuel McFadzean, William Smith, Damien McGrouther, Sophie Collin, Nicolas Reyren, Vincent Cros, Christopher H. Marrows, and Stephen McVitie**

S1. FIB patterning

Three methods of creating point-like defects with the FIB were trialled, two using ‘patterning routines’ and one using streamfiles. The patterning routines are part of the standard software which operates the FEI Nova NanoLab 200 SEM and FIB; they allow the user to draw a set of standard shapes that the ion beam then rasters over using a path which is predesignated by the chosen tool. We used the line tool which rasters the ion beam linearly along the length of the line defined by the user, and the circle tool which moves the the ion beam in a spiral motion inside the circle defined by the user. Conversely, streamfiles are a user-written list of dwell times and beam coordinates which precisely define the beam scan path. To create point-like FIB defects the line tool was set to irradiate a 10 nm line, the circle tool to irradiate a 10 nm diameter circle, and a one-line streamfile written to irradiate precisely one point. Figure S1 shows three defects, each associated with a notational dose of 1×10^{18} ions/cm^2 (as determined by the beam current, dwell time and number of passes), created from; (a) a streamfile, (b) the line pattern tool and (c) the circle pattern tool. There is obvious damage associated with (a), whilst for (b) and (c) holes are milled, with the latter significantly larger. As in the main text of the paper, these defects were made with a 30 keV Ga^+ ion beam, with current 10 pA to give a 10 nm probe.

All defects reported in the main paper were produced using procedure in Figure S1(a) (which irradiates a single point), apart from Figure 3 where the procedure in Figure S1(c) produced larger defects which were used to illustrate the contrast from a skyrmions versus the contrast from a defect. We point out the difference in notional dose using preset methods available on the FIB software which for S1(b) and S1(c) result in a higher dose and larger lateral defect as, effectively, the beam is scanned at multiple overlapping positions. We suspect the severity of this effect to be enhanced when creating objects on the order of the beam diameter. This idea is sketched above the SEM images in Figure S1 where the diffuse red dot represents the ion beam and the black dot shows its centre. The difference in opacity of the graphics represents the unintended higher ‘effective’ dose caused by beam overlap. Furthermore, this effect could be lessened by reducing the beam overlap parameter; the default value is 50% and intended to deliver constant dose over the pattern despite the Gaussian shape of the beam.

To give context on the magnitude of the discrepancy in delivered dose discussed in this section, using the procedure in S1(a) (with no beam overlap and therefore unambiguous determination of dose) a 70 nm diameter hole is milled with a dose of 5×10^{18} ions/cm^2. This is compared to the 60 and 110 nm diameter holes milled with the procedures in S1(b, c) respectively with a notational ion dose of 1×10^{18} ions/cm^2.

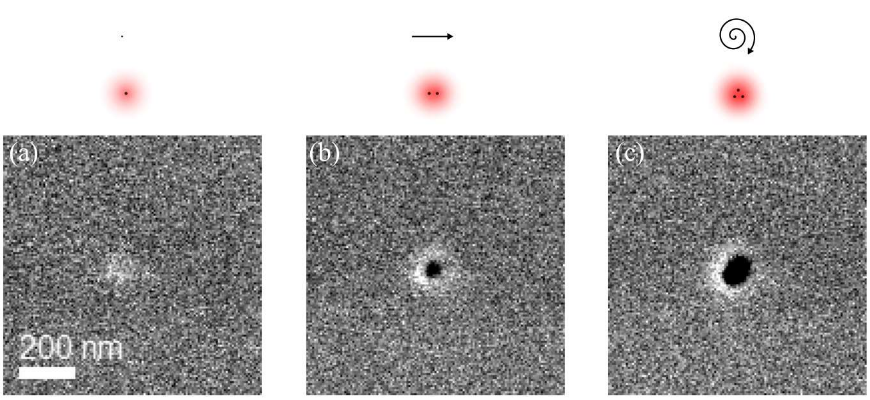

Figure S1. SEM images of point defects created with different methods on FIB with identical beam current, dwell time and number of passes: (a) irradiation of a single point with stream file, (b) 10 nm line with in-built line tool and (c) 10 nm diameter circle with in-built circle tool.

S2. Skyrmion size analysis

As mentioned in the main text, the diameter of a Néel skyrmion can be measured quantitatively from Fresnel images by measuring the distance between the maximum of the peak and minimum of the trough of the skyrmion contrast. For Néel skyrmions, the Fresnel image contrast arises from M_z[1–4] and principally relates to the gradient of the magnetisation, consequently the positions of the extrema in the Fresnel contrast effectively give the positions where $M_z = 0$. Therefore, with this measurement method, we define the skyrmion diameter to be the diameter of the circle where $M_z = 0$. In Figure S2 we present graphs of out of plane applied field versus the skyrmion size from (a) sample 1 unmodified, (b) sample 1 with defects and (c) sample 2 with defects. For all graphs, each data point is the mean of five measurements and the error bar is the standard error on the mean. Additionally, all graphs show a similar level of skyrmion compression with field.

Figure S2(a) shows the mean skyrmion size over the full field range they are present: they are first observed in -50 mT until -80 mT. Figures S2(b,c) are measured only from the key areas of the charts in Figure 4 of the main text outlined in red which correspond to 100% skyrmion nucleation and are recorded independently for defects of different dose.

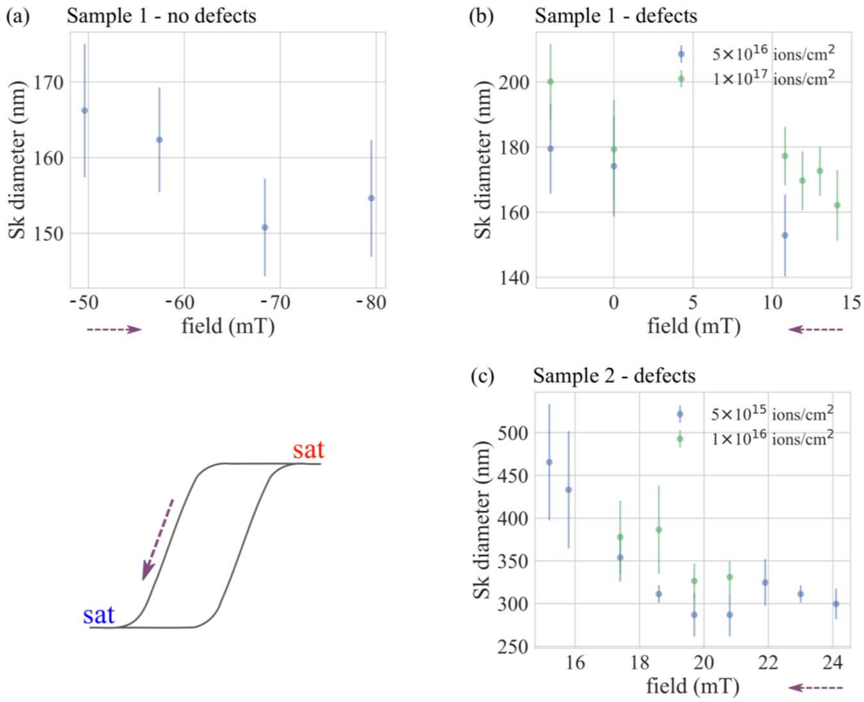

Figure S2. Evolution of the skyrmion size with applied field for (a) skyrmions naturally supported in sample 1, skyrmions nucleated at artifical defects on (b) sample 1 and (c) sample 2.

S3. Interpreting DPC imaged of Néel-type skyrmions

As mentioned in the preceding section, the in-plane magnetisation associated with Néel-type objects (walls and skyrmions) does not contribute to Lorentz microscopy images.[1–4] Therefore, for simplicity and without lack of accuracy, the following discussion involves only the domain magnetisation M_z. Lorentz microscopy is sensitive to the $\boldsymbol{B}_\perp$, the magnetic induction perpendicular to the electron beam trajectory, integrated through the sample thickness. As discussed in the main text (and the references provided above), this means perpendicularly magnetised materials must be tilted to produce any contrast in Lorentz microscopy images. Both the sensitivity to $\boldsymbol{B}_\perp$ (not $\boldsymbol{M}$) and the necessity to tilt, leads to elliptical contrast from a circular Néel skyrmion in DPC images.

Figures S3(a) and (b) depict the geometry of a skyrmion containing sample (in cross-section) in the TEM both in untilted and tilted positions respectively, where the electrons travel along $+\hat{\boldsymbol{z}}$. Tilting the structure and projecting back on the *xy* plane (i.e. a detector in the microscope) leads to contraction of the object in the direction perpendicular to the tilt axis. For a circular skyrmion, represented only by its M_z component Figure S3(d), this results in an elliptical shaped magnetisation corresponding to the skyrmion, see Figure S3(e). As denoted by the red arrows in S3(e), a component $sin(\theta)$ of the original sample M_z is projected in the *xy* plane of the microscope. The skyrmion is associated with a stray field $\boldsymbol{H}$ as well as magnetisation $\boldsymbol{M}$, as sketched in Figure S3(c). DPC images are then this dipole-like $\boldsymbol{B}$ (= $\mu_0(\boldsymbol{M} + \boldsymbol{H})$) field projected through the sample thickness onto the *xy* plane. The $\boldsymbol{H}$ field cancels much of the $\boldsymbol{M}$ sketched in Figure S3(e), preferentially reducing the DPC contrast perpendicular to the tilt axis again leading to elliptical contrast. Note that sense of ellipticity in Figure S3(e) is orthogonal to the ellipticity caused by contraction. Parallel to the tilt axis, the skyrmion size is undistorted (as highlighted by the yellow dashed line).

The DPC image simulation was designed to accurately represent the experimental conditions. This uses an M_z configuration constructed to represent the skyrmion imaged in Figure 5 of the main paper. This is a circle of diameter 150 nm with a narrow transitional wall (between $\pm M_z$) matched to the width of the profile in Figure 5(b) - and is calculated at a tilt of 24.6°. If one were to ignore the effect of the stray field (i.e. assuming the contrast only arises from the magnetisation in the sample), the difference between the maximum and minimum values in the DPC image (which occur parallel to the tilt axis) would correspond to $2B_s t\tan(\theta)$ where $B_s = \mu_0 M_s$. For a tilt of 24.6°, this is 0.92 $B_s t$. In the simulation, where the effects of the stray field are properly accounted for, the difference between the maximum and minimum values in the DPC image is measured as 0.76 $B_s t$. Therefore, in order to extract B_s (and M_s) experimentally we apply a stray-field-compensating
scaling factor of (0.76/0.92 =) 0.83.

In conclusion, three things should be understood: DPC images of perfectly circularly symmetric skyrmions have elliptical contrast; in the direction perpendicular to the tilt axis, the skyrmion diameter can be measured, as can M_s (assuming the sample thickness is known). The DPC image calculation is of a perfect system, with no sources of contrast other than the smoothly varying magnetisation. The real samples are polycrystalline, therefore DPC images also contain shorter-range electrostatic grain contrast as well as contrast from the skyrmion. Consequently, the experimental DPC image in Figure 5(a) of the main text has significant background undulations but otherwise matches Figure S3(f) very well.

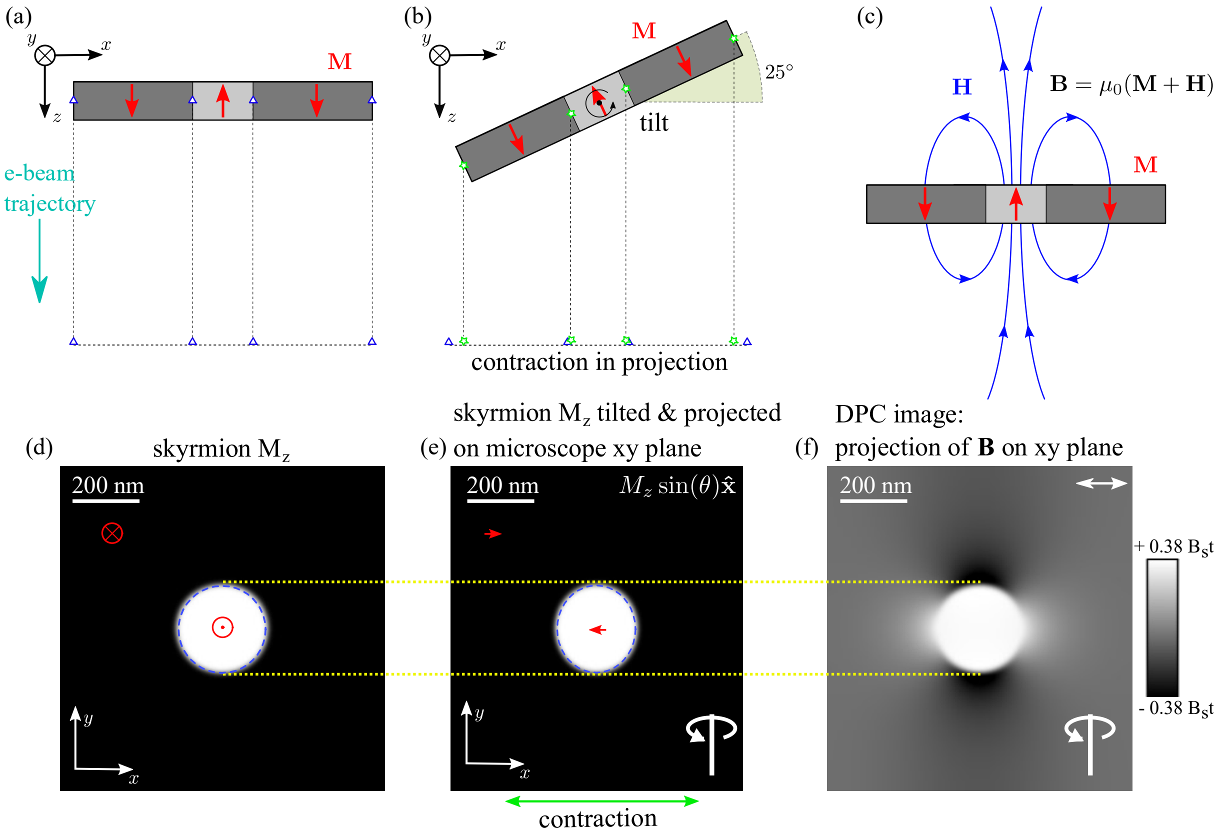

Figure S3. (a) geometry of skyrmion sample (depicted in cross-section) in a TEM at normal incidence to the electrons travelling along the $+\hat{\boldsymbol{z}}$ direction. (b) geometry of skyrmion sample tilted by 24.6° around an axis along y direction: the object is contracted in the *x* direction when projected back onto the *xy* plane (i.e. when forming an image on a detector in the TEM). (c) a skyrmion is associated with a dipole-like ***B*** field consisting of the magnetisation ***M*** and the stray field ***H***. Consider (d) the M_z of a skyrmion, when tilted and projected onto the *xy* plane, a component *sin(θ)* of is M_z projected onto the *xy* plane and the shape is distorted to an ellipse (e). (f) DPC images ***B*** (***H*** + ***M***) and, at the skyrmion parallel to the tilt axis, ***H*** and ***M*** cancel significantly leading to an exaggerated elliptical. Note that the ellipse in (e) is not seen in (f) which appears elliptical in an orthogonal direction.

References

[1] M. J. Benitez, A. Hrabec, A. P. Mihai, T. A. Moore, G. Burnell, D. McGrouther, C. H. Marrows, S. McVitie, *Nat. Commun.* **2015**, *6*, 8957.

[2] S. McVitie, S. Hughes, K. Fallon, S. McFadzean, D. McGrouther, M. Krajnak, W. Legrand, D. Maccariello, S. Collin, K. Garcia, N. Reyren, V. Cros, A. Fert, K. Zeissler, C. H. Marrows, *Sci. Rep.* **2018**, *8*, 5703.

[3] W. Jiang, S. Zhang, X. Wang, C. Phatak, Q. Wang, W. Zhang, M. B. Jungfleisch, J. E. Pearson, Y. Liu, J. Zang, X. Cheng, A. Petford-Long, A. Hoffmann, S. G. E. te Velthuis, *Phys. Rev. B* **2019**, *99*, 104402.

[4] K. Fallon, S. McVitie, W. Legrand, F. Ajejas, D. Maccariello, S. Collin, V. Cros, N. Reyren, *Phys. Rev. B* **2019**, 100, 214431.